Nanoscale

PAPER

View Article Online
View Journal | View Issue

Cite this: *Nanoscale*, 2019, **11**, 17815

High-performance electrochromic films with fast switching times using transparent/conductive nanoparticle-modulated charge transfer†

Junsang Yun,‡ Yongkwon Song,‡ Ikjun Cho, Yongmin Ko, Cheong Hoon Kwon and Jinhan Cho *

One of the most critical issues in electrochromic (EC) films based on transition metal oxides such as tungsten oxides (WO_x) is their poor charge transfer property, which is closely related to EC performance. Herein, high-performance EC films with enhanced charge transport are prepared using small-molecule linkers and transparent/conductive nanoparticles (NPs). In this work, oleylamine (OAm)-stabilized $WO_{2.72}$ nanorods (NRs) and OAm-stabilized indium tin oxide (ITO) NPs are layer-by-layer (LbL)-assembled with small-molecule linkers (tris(2-aminoethyl)amine, TREN) using a ligand-exchange reaction between bulky/insulating OAm ligands and TREN molecules. In this case, there is only one TREN layer between neighboring inorganic components ($WO_{2.72}$ NRs and/or ITO NPs), resulting in a dramatic decrease in the separation distance. This minimized separation distance as well as the periodic insertion of transparent/conductive ITO NPs can significantly reduce the charge transfer resistance within $WO_{2.72}$ NR-based EC films, which remarkably improves their EC performance. Compared to EC films without ITO NPs, the formed EC films with ITO NPs exhibit faster switching responses (4.1 times in coloration time and 3.5 times in bleaching time) and a maximum optical modulation of approximately 55.8%. These results suggest that electrochemical performance, including EC performance, can be significantly improved through structural/interfacial designing of nanocomposites.

Received 23rd July 2019,
Accepted 2nd September 2019

DOI: 10.1039/c9nr06259a

rsc.li/nanoscale

1. Introduction

Electrochromic (EC) materials, which exhibit reversible electrochemical reaction (*i.e.*, redox state switching)-stimulated color changes under an external electric potential, have attracted significant attention for their use in various applications, such as energy-saving smart windows, displays, reflectance mirrors, and gas sensors.[1–10] In particular, among the variety of EC materials, inorganic tungsten oxides (WO_x) with multiple oxidation states have been considered to be one of the most promising candidates due to their outstanding EC performance, including high color contrast (*i.e.*, optical modulation), fast switching times (*i.e.*, coloration/bleaching times), high coloration efficiencies, good chemical stability, and relatively good electrical conductivity (10–10^{-6} S cm^{-1}).[11–21] Generally, it is widely accepted that the reversible EC mechanism of WO_x in a lithium electrolyte is associated with the insertion/extraction of Li^+ ions and electrons as follows:[13–15]

$$WO_x\ (\text{bleached state}) + yLi^+ + ye^- \leftrightarrow Li_yWO_x\ (\text{colored state}) \quad (1)$$

In particular, it has been reported that WO_x with nonstoichiometric compositions ($2 \leq x \leq 3$), mainly the stoichiometry of $WO_{2.72}$ ($W_{18}O_{49}$), can exhibit better EC performance than saturated WO_3 because oxygen vacancy defects in WO_x can improve their electrical conductivity and provide more active sites for Li^+ ions.[18–20]

Although the kinetics of Li^+ ion intercalation and the resulting EC performance strongly depend on the crystalline structure of WO_x (*i.e.*, ion diffusion coefficient),[15–18] the ion diffusion length, governed by the total thickness (or loading amount) and architecture of EC films, also plays an important role in determining EC performance indices.[20,22–30] More specifically, in the case of nonporous/compact EC films, an increase in the film thickness to obtain deeper color changes can lead to longer switching times, which are mainly caused by the increased diffusion pathway for Li^+ ions between the outermost surface and the interior of the EC films. On the other hand, the propagation of Li^+ ions in porous EC films is

Department of Chemical & Biological Engineering, Korea University, 145 Anam-ro, Seongbuk-gu, Seoul 02841, Republic of Korea. E-mail: jinhan71@korea.ac.kr

†Electronic supplementary information (ESI) available. See DOI: 10.1039/c9nr06259a

‡These authors contributed equally to this work.

much faster than that in nonporous EC films in a given time range, implying faster switching times. That is, the trade-off relationship between the thickness (or loading amount) for color changes and switching times in EC films can be considerably mitigated through the construction of porous structures allowing facile Li^+ ion transport. Furthermore, compared with nonporous EC films, EC films with a porous structure can provide a larger active surface area with the electrolyte and enhance the durability by alleviating the expansion/contraction of WO_x during the repetitive insertion/extraction of Li^+ ions.[22] For these reasons, one-dimensional (1D) WO_x nanorods (NRs) or nanowires (NWs) have mainly been used for preparing highly porous EC films because their intrinsic morphology with a large aspect ratio can lead to the formation of a random packing-induced porous structure during assembly processes.[25–30]

The electrical conductivity of WO_x-based EC films can also have a significant effect on their EC performance (particularly switching times for coloration/bleaching). Given that the electrochromism of WO_x originates from the insertion/extraction of Li^+ ions and electrons during a cathodic scan (for Li_yWO_x with a colored state) and an anodic scan (for WO_x with a bleached state), the switching times strongly depend on the electron transport within EC films as well as the ion transport. Although the electrical conductivity of WO_x can slightly increase with increasing oxygen vacancy concentration, such as n-type doping,[19,31] the incorporation of additional conductive components into WO_x-based EC films can significantly improve the EC performance by lowering the charge transfer resistance. However, it has been difficult to achieve the uniform nanoblending between WO_x NRs (or NWs) and conductive materials (*e.g.*, conductive polymers, metal nanomaterials, or carbon nanotubes (CNTs)) using solution-based processes due to the presence of bulky organic ligands bound to the surface of WO_x NRs. That is, unfavorable interfacial interactions between the hydrophobic organic ligands of WO_x NRs and conductive components induce phase separation or agglomeration within EC films, which can exert an adverse effect on the EC operations and optical transparency of EC films.[32] Additionally, the use of nontransparent conductive components such as CNTs and metal nanomaterials significantly reduces the optical transmittance of EC films in a bleached state.[33] Furthermore, it should be noted that bulky/insulating organic ligands within WO_x-based EC films severely limit electron transport in various electrochemical applications, including electrochromism.[16,28,30] Accordingly, if transparent and conductive nanoparticles (NPs), such as indium tin oxide (ITO) NPs, can be uniformly incorporated into porous WO_x-based EC films through stable/favorable interfacial interactions and if the bulky organic ligands capped on WO_x nanomaterials can be effectively removed during an assembly process, we envision that the performance of the resultant EC films will be significantly improved compared to that of pristine WO_x-based EC films by reducing the charge transfer resistance.

Layer-by-layer (LbL) assembly based on complementary interactions (mainly electrostatic interactions) between neighboring components has been demonstrated as a potentially versatile and well-established methodology for precise control over functionality, thickness (or loading amount), and chemical composition.[34–46] With the aid of conventional electrostatic LbL assembly carried out in aqueous media, a variety of conductive EC polymers, including poly(3,4-ethylenedioxythiophene):poly(styrene sulfonate) (PEDOT:PSS) and polyaniline (PANI), have been mainly assembled to prepare EC films.[29,30,43–46] For example, Cui *et al.* reported that electrostatic LbL-assembled porous EC films composed of cationic PANI and anionic polyelectrolyte complexes exhibited notably fast switching behavior (coloration time (t_c) ~ 3 s and bleaching time (t_b) ~ 15 s) and optical modulation (ΔT) of 28.7%.[44] Additionally, Li *et al.* reported that electrostatic LbL-assembled films composed of $(W_{0.71}Mo_{0.29}O_3$ NR/PEDOT:PSS$)_n$ multilayers displayed higher EC performance than neat $W_{0.71}Mo_{0.29}O_3$ NR-based EC films.[30] However, the conjugated backbones of EC polymers are known to be unstable toward atmospheric oxygen or moisture in the charged state, which restricts their practical applications in EC devices.[21] Furthermore, the electrochemically inactive/bulky polymer linkers and the low packing density (<30%) due to reciprocal electrostatic repulsion between the same charged components are still the major obstacles to obtaining high-performance EC films *via* conventional electrostatic LbL assembly.[30,40]

Herein, we introduce a high-performance EC film composed of electrochromic transition metal oxide NRs, transparent/conductive NPs, and small-molecule linkers using unconventional LbL assembly in organic media. We highlight that our approach can considerably improve optical modulations and switching times for coloration/bleaching by facilitating charge transport within EC films. For this study, the as-synthesized oleylamine (OAm)-stabilized $WO_{2.72}$ NRs (OAm-$WO_{2.72}$ NRs) and OAm-stabilized ITO NPs (OAm-ITO NPs) were consecutively deposited with small amine-functionalized molecules (tris(2-aminoethyl)amine, TREN) (Fig. 1). (*Caution: the real internal structure of the nanocomposite film composed of $WO_{2.72}$ NRs and ITO NPs was nanoblended and mixed due to the formation of randomly deposited $WO_{2.72}$ NR and ITO NP layers. The suggested scheme was simply depicted for the build-up of multilayers. The more detailed explanation will be given in the latter part.*) In this case, the bulky/insulating OAm ligands loosely bound to the surface of the $WO_{2.72}$ NRs and ITO NPs were almost completely replaced by small TREN molecules through a ligand-exchange reaction. Additionally, during LbL assembly, the randomly and densely packed $WO_{2.72}$ NRs generated a porous structure, allowing the facile ion transport and effective incorporation of transparent/conductive NPs. Importantly, the small-molecule linkers also substantially minimized the separation distance between neighboring inorganic components (*i.e.*, $WO_{2.72}$ NRs and ITO NPs), which decreased the charge transfer resistance within the EC films. By virtue of this unique adsorption behavior, the $WO_{2.72}$ NR-based EC films obtained by using small-molecule linkers (*i.e.*, $(WO_{2.72}$ NR/TREN$)_{20}$ multilayers) exhibited higher EC performance (t_c ~ 12.2 s and t_b ~ 6.5 s)

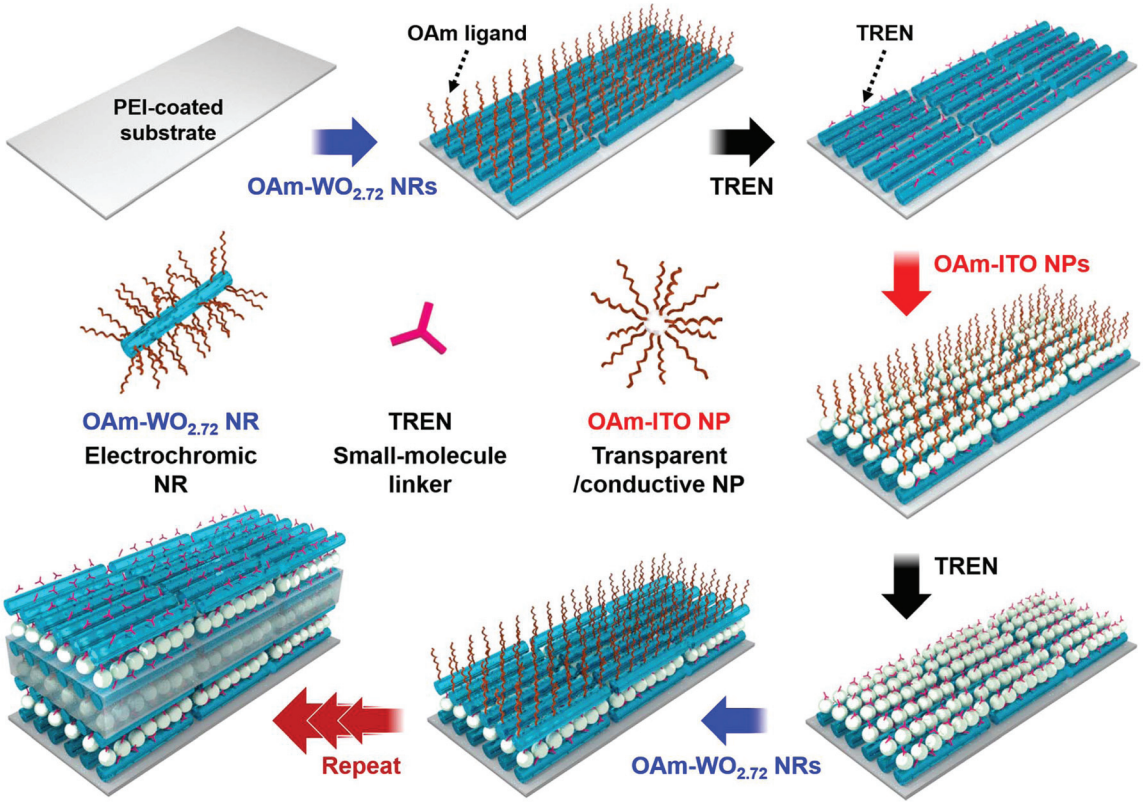

Fig. 1 Schematic illustration of the formation of EC nanocomposite films based on electrochromic $WO_{2.72}$ NRs and transparent/conductive ITO NPs by unconventional LbL assembly using small-molecule linkers. Although the formation of sharp and aligned interfaces between $WO_{2.72}$ NR and ITO NP layers was virtually depicted in the scheme, the real internal structure of the LbL-assembled film was nanoblended and mixed layer structure due to the formation of randomly packed $WO_{2.72}$ NR layers with a porous structure.

than the EC films obtained by using bulky polymer linkers (*i.e.*, $(WO_{2.72}$ NR/polymer$)_{20}$ multilayers) ($t_c \sim 23.3$ s and $t_b \sim 17.6$ s).

Furthermore, the EC performance of the $(WO_{2.72}$ NR/TREN$)_n$ multilayers was dramatically enhanced by the incorporation of transparent/conductive ITO NPs into the multilayers. It is particularly worth noting that the inserted ITO NPs facilitate charge transport without causing a notable decrease in optical transmittance in the bleached state. That is, when the ITO NPs were periodically inserted into the multilayers (*i.e.*, $(WO_{2.72}$ NR/TREN/ITO NP/TREN$)_m$ multilayers), the t_c, t_b, and ΔT of the EC films with $m = 20$ were changed from 12.2 s, 6.5 s, and 33.3% (without ITO NPs) to 5.0 s, 3.3 s, and 41.6% (with ITO NPs), respectively. In the case of the EC films with $m = 40$, the t_c, t_b, and ΔT were sharply changed from 44.2 s, 53.2 s, and 50.3% (without ITO NPs) to 10.9 s, 15.2 s, and 55.8% (with ITO NPs), respectively. Given that the periodic incorporation of ITO NPs, the use of small-molecule linkers, and the unique nanocomposite structural/interfacial design have significant effects on the charge transport within transition metal oxide-based films, we believe that our combined approach can provide an important basis for preparing a variety of high-performance electrochemical devices, including EC films.

2. Experimental section

2.1. Materials

Tungsten hexacarbonyl (99.99%), trimethylamine *N*-oxide dihydrate (≥99.0%), oleylamine (OAm, 70%), indium(III) acetate (99.99%), tin(II) ethylhexanoate (92.5–100%), *n*-octanoic acid (≥99%), dioctyl ether (99%), polyethylenimine (PEI, branched), and tris(2-aminoethyl)amine (TREN, 96%) were purchased from Sigma-Aldrich and used without additional purification. Solvents such as toluene (99.5%) and ethanol (94.5%) were purchased from Daejung Chemicals & Metals Co., Ltd (Republic of Korea).

2.2. Synthesis of OAm-$WO_{2.72}$ NRs

OAm-$WO_{2.72}$ NRs in toluene were synthesized as previously reported by Lee *et al.*[47] Tungsten hexacarbonyl (2 mmol), trimethylamine *N*-oxide dihydrate (12 mmol), and OAm (32 mmol) were mixed in a 100 mL Schlenk tube with vigorous stirring. The reaction mixture was heated in an oil bath from room temperature to 270 °C for 2 hours under a flow of Ar gas. Next, the viscous reaction mixture with a deep blue color went through additional aging at 270 °C for 24 hours. Then, the mixture was cooled to room temperature and centrifuged (8000 rpm, 10 min, 20 °C) several times with excess ethanol to

remove residual impurities. The resultant blue OAm-$WO_{2.72}$ NR powder was dispersed in toluene. Finally, the OAm-$WO_{2.72}$ NR solution was used after removing any larger NRs through an additional centrifugation step (6000 rpm, 10 min, 20 °C).

2.3. Synthesis of OAm-ITO NPs

OAm-ITO NPs in toluene were prepared using a method reported by Kanehara *et al.*[48] In brief, 1.08 mmol of indium(III) acetate, 0.12 mmol of tin(II) ethylhexanoate, 3.6 mmol of *n*-octanoic acid, 30 mmol of OAm, and 10 mL of dioctyl ether were added into a three-necked flask under vigorous stirring. After heating the reaction mixture at 80 °C for 30 min under vacuum, the mixture was heated at 150 °C for 1 hour under an Ar atmosphere. Subsequently, the mixture was heated at 280 °C for 2 hours to form the NPs and cooled to room temperature. Centrifugal purification (8000 rpm, 10 min, 20 °C) with excess ethanol was repeated several times to obtain pure OAm-ITO NP precipitates. Finally, the obtained precipitates were dissolved in toluene and centrifuged (6000 rpm, 10 min, 20 °C) to obtain a uniform size distribution.

2.4. Assembly of ($WO_{2.72}$ NR or ITO NP/TREN)$_n$ multilayers

All substrates, such as Si wafers, quartz glasses, gold-sputtered Si wafers (for FTIR analysis), QCM electrodes and fluorine-doped tin oxide (FTO) glasses, were surface-treated by irradiation with UV light ($\lambda \sim 350$ nm) for 10 min and then dipped into a solution of amine-functionalized PEI in ethanol (1 mg mL^{-1}, $M_w \sim 800$) for 20 min. After being dipped into the PEI solution, the substrates were gently washed with pure ethanol to eliminate weakly adsorbed PEI and dried under an air stream. Next, the PEI-coated substrates were immersed in a solution of OAm-$WO_{2.72}$ NRs (or OAm-ITO NPs) in toluene (10 mg mL^{-1}) for 20 min, washed with pure toluene, and dried under an air stream. Subsequently, the OAm-$WO_{2.72}$ NR-coated substrates were dipped into a solution of TREN in ethanol (1 mg mL^{-1}) for 20 min and were subjected to a similar process of washing with pure ethanol and drying with an air stream. These dipping cycles were repeated until the desired number of multilayers was acquired.

2.5. Characterization

The size distribution and crystal structure of OAm-$WO_{2.72}$ NRs and OAm-ITO NPs were examined using HR-TEM (Tecnai 20, FEI). The crystallinity of OAm-$WO_{2.72}$ NRs was also observed from the XRD patterns obtained using a SmartLab instrument (Rigaku) with Cu K_α radiation. The binding energies of OAm-$WO_{2.72}$ NRs were investigated using XPS (X-TOOL, ULVAC-PHI) with Al K_α radiation. To confirm the occurrence of a ligand-exchange reaction, the vibrational spectra of multilayers were measured by FTIR spectroscopy (CARY 600, Agilent Technologies) in ATR mode. The obtained raw data were smoothed after baseline correction using spectral analysis software (OMNIC 9, Thermo Scientific) and plotted. The qualitative and quantitative growth behaviors of the multilayers were observed using a UV-vis spectrophotometer (Lambda 35, PerkinElmer) in the spectral range from 200 nm to 1000 nm and a QCM (QCM 200, SRS), respectively. Mass changes (Δm) in multilayers were calculated from frequency changes ($-\Delta F$) in QCM measurements using the Sauerbrey equation as follows.[40]

$$\Delta F\ (\mathrm{Hz}) = -\frac{2{F_0}^2}{A\sqrt{\rho_q \mu_q}} \times \Delta m \quad (2)$$

In eqn (2), F_0, A, ρ_q, and μ_q correspond to the fundamental resonance frequency (5 MHz), the area, the density (2.65 g cm^{-3}), and the shear modulus (2.95×10^{11} g cm^{-1} s^{-2}) of the QCM electrodes, respectively. Consequently, eqn (2) can be simplified by substituting the values and expressed as eqn (3)

$$-\Delta F\ (\mathrm{Hz}) = 56.6 \times \Delta m_A \quad (3)$$

where Δm_A indicates the mass change per unit area (μg cm^{-2}). Finally, the surface morphology, total thickness, and EDS images of the multilayers were observed using an FE-SEM (S-4800, Hitachi).

2.6. Electrochemical/EC measurements

All electrochemical measurements, including CV and EIS, were carried out with an Ivium-n-Stat electrochemical workstation (Ivium Technologies). The electrochemical properties of $WO_{2.72}$ NR-based EC films with ITO NPs or without ITO NPs (working electrodes, active area ~3 cm^2) were estimated using a three-electrode cell configuration composed of a Ag/AgCl electrode in propylene carbonate (reference electrode) and Pt wire (counter electrode). $LiClO_4$ dissolved in propylene carbonate (1 mol L^{-1}) was used as the electrolyte. CV scans were conducted in the potential range from −1.0 V to +1.0 V, and EIS analyses were performed in the frequency range from 0.1 Hz to 100 kHz with a perturbation amplitude of 0.01 V. For EC operation, the chronoamperometry mode in Ivium-n-Stat was used to apply constant potentials (+4.0 V for bleaching and −4.0 V for coloration) to $WO_{2.72}$ NR-based EC films with ITO NPs or without ITO NPs. Simultaneously, optical transmittance spectra were recorded in real time across a wavelength range from 200 nm to 1000 nm using a UV-vis spectrophotometer (Lambda 35). In the EC switching experiment measuring the response times for bleaching/coloration, the optical transmittance at a visible wavelength of 633 nm was measured while alternately applying potentials of ±4.0 V for 30 s (m, n = 10, 20) or 120 s (m, n = 30, 40) intervals.

3. Results and discussion

3.1. Preparation of ($WO_{2.72}$ NR/TREN)$_n$ multilayers

For the preparation of EC nanocomposite films based on WO_x nanomaterials, we first synthesized highly uniform OAm-$WO_{2.72}$ NRs.[47] The as-prepared OAm-$WO_{2.72}$ NRs exhibited a diameter of 4.0 ± 1.5 nm and a length of 39 ± 9.0 nm (aspect ratio ~10) with good dispersibility in nonpolar solvents such as hexane and toluene (Fig. 2a). A high-resolution transmission electron microscopy (HR-TEM) image of the OAm-

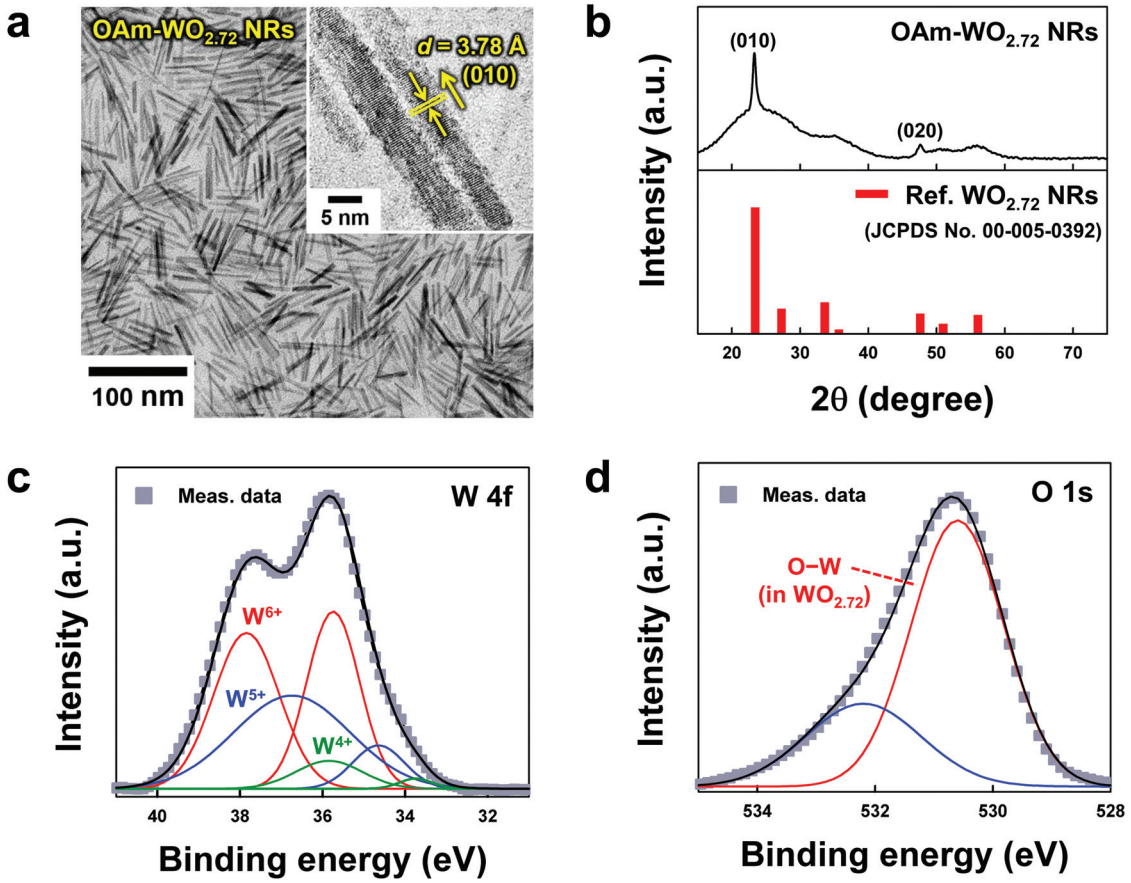

Fig. 2 (a) HR-TEM images of OAm-$WO_{2.72}$ NRs dispersed in toluene. The inset shows that OAm-$WO_{2.72}$ NRs have a lattice spacing (d) found to be approximately 3.78 Å, which corresponds to the (010) plane of a monoclinic $WO_{2.72}$ phase. (b) XRD patterns of the as-prepared OAm-$WO_{2.72}$ NRs (top) and $WO_{2.72}$ reflections (bottom; JCPDS No. 00-005-0392). Deconvoluted XPS spectra of (c) W 4f and (d) O 1s collected from OAm-$WO_{2.72}$ NRs.

$WO_{2.72}$ NRs displayed a well-formed crystal structure with a lattice spacing (d) of 3.78 Å along the direction of NR growth, which agreed with the (010) plane of a monoclinic $WO_{2.72}$ phase (see the inset in Fig. 2a).[49] In particular, evident (010) and (020) peaks of the OAm-$WO_{2.72}$ NRs were observed in the X-ray diffraction (XRD) pattern, indicating the formation of a highly crystalline structure grown in one direction (Fig. 2b). Furthermore, to obtain a better understanding of the chemical states of the prepared OAm-$WO_{2.72}$ NRs, we investigated their binding energies using X-ray photoelectron spectroscopy (XPS). Fig. 2c shows that the deconvoluted tungsten (W) atom 4f core level spectra of the OAm-$WO_{2.72}$ NRs could be divided into three doublets that correspond to the three different oxidation states of tungsten atoms. The main peaks in the W 4f spectrum originated from W^{6+} $4f_{7/2}$ and W^{6+} $4f_{5/2}$ (*i.e.*, the stoichiometry of WO_3), and the other peaks indicated the presence of oxygen vacancy states such as W^{5+} and W^{4+}. More specifically, the peaks at 35.7 and 37.8 eV in the XPS spectra represented the emissions from W $4f_{7/2}$ and W $4f_{5/2}$ levels in the W^{6+} oxidation state, respectively. Additionally, the peaks at 34.6 and 36.7 eV originated from the W^{5+} oxidation state (W^{5+} $4f_{7/2}$ and W^{5+} $4f_{5/2}$ levels, respectively), and the peaks at 33.7 and 35.8 eV originated from the W^{4+} oxidation state (W^{4+} $4f_{7/2}$ and W^{4+} $4f_{5/2}$ levels, respectively). The proportions of the W^{6+}, W^{5+}, and W^{4+} oxidation states among the tungsten atoms were estimated to be approximately 57.2%, 36.6%, and 6.2%, respectively. Deconvoluted oxygen (O) atom 1s XPS spectra are also shown in Fig. 2d. The peak at 530.6 eV was derived from the oxygen bonds in the $WO_{2.72}$ NRs, and the peak at 532.2 eV was attributed to the oxygen bonds in various impurities, such as OAm ligands attached onto the surface of the $WO_{2.72}$ NRs. These results suggest that the as-prepared OAm-$WO_{2.72}$ NRs exactly coincided with the nonstoichiometric $WO_{2.72}$ phase reported in a previous study.[50]

On the basis of these results, $(WO_{2.72}$ NR/TREN$)_n$ multilayers were prepared using the OAm-$WO_{2.72}$ NRs and small-molecule linkers (TREN). In this case, the multidentate TREN molecules, which have three primary amine groups ($-NH_2$) in one molecule, have a higher affinity for the surface of the $WO_{2.72}$ NRs through multiple coordination bonds than monodentate OAm ligands.[51] Therefore, the bulky/insulating OAm ligands on the surface of the $WO_{2.72}$ NRs could be replaced by small TREN molecules during LbL deposition. To confirm this ligand-exchange reaction, the residual OAm ligands in the

LbL-grown $(WO_{2.72}$ NR/TREN$)_n$ multilayers were examined as a function of the bilayer number (n) by Fourier transform infrared (FTIR) spectroscopy in attenuated total reflection (ATR) mode (Fig. 3a and S1†). In the FTIR spectrum of pristine OAm-$WO_{2.72}$ NRs, we detected distinct absorption peaks assigned to W–O stretching (attributed to the $WO_{2.72}$ NRs) at 927 and 870 cm^{-1} and C–H stretching (attributed to the long alkyl chains of the OAm ligands) at 2926 and 2854 cm^{-1}.[28,52] In the

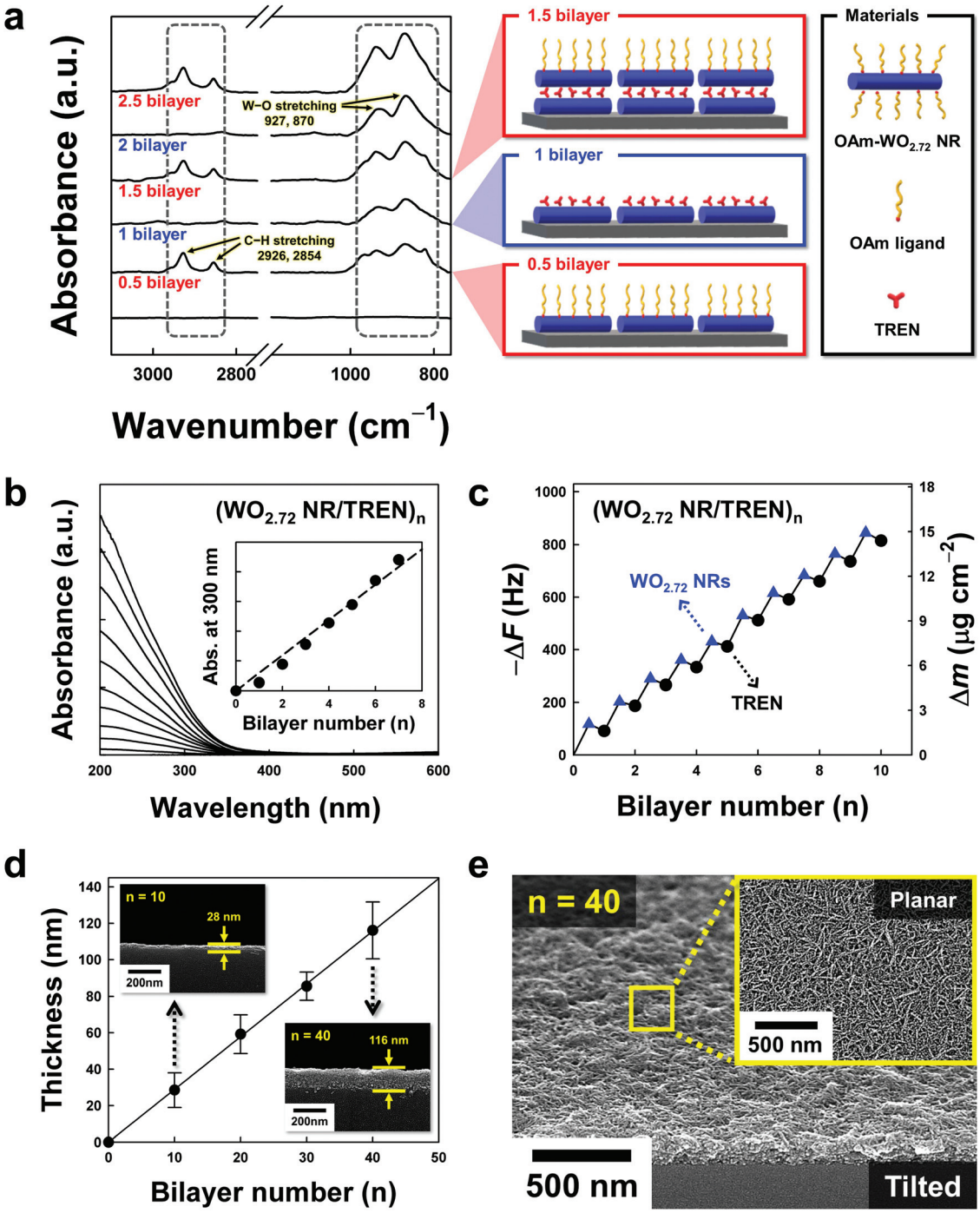

Fig. 3 (a) ATR-FTIR spectra and schematic representation of $(WO_{2.72}$ NR/TREN$)_n$ multilayers as a function of the bilayer number (n). (b) UV-vis absorbance spectra of $(WO_{2.72}$ NR/TREN$)_n$ multilayers with an increase in the bilayer number. The inset shows the absorbance of multilayers at a wavelength of 300 nm, indicating the linear and regular vertical growth of the films. (c) Frequency and mass changes of $(WO_{2.72}$ NR/TREN$)_n$ multilayers obtained from QCM measurements as a function of the bilayer number. (d) Total thickness change of $(WO_{2.72}$ NR/TREN$)_n$ multilayers measured from cross-sectional FE-SEM images (insets) with increasing the bilayer number from 10 to 40. (e) Tilted and planar (inset) FE-SEM images of $(WO_{2.72}$ NR/TREN$)_{40}$ multilayers.

case of pristine TREN, no significant absorption peak was observed in the above-mentioned wavelength ranges. Thus, when the OAm-$WO_{2.72}$ NRs were deposited onto amine-functionalized substrates, the two noticeable C–H stretching peaks (attributed to the OAm ligands) as well as the W–O stretching peaks (attributed to the $WO_{2.72}$ NRs) appeared in the spectrum of the OAm-$WO_{2.72}$ NR layer-coated substrates (see the FTIR spectrum referred to as "0.5 bilayer"). Subsequently, when TREN was further adsorbed onto the outermost OAm-$WO_{2.72}$ NR layer-coated substrates, the C–H stretching peaks became barely detectable, whereas the intensity of the W–O stretching peaks was maintained without any notable change (see the FTIR spectrum referred to as "1 bilayer"), implying a ligand-exchange reaction between the OAm ligands and TREN. Additional deposition of the OAm-$WO_{2.72}$ NRs onto the $(WO_{2.72}$ NR/TREN$)_1$-coated substrates regenerated the C–H stretching peaks and further increased the intensity of the W–O stretching peaks (see the FTIR spectrum referred to as "1.5 bilayer"). That is, the alternating depositions of OAm-$WO_{2.72}$ NRs and TREN produced inversely correlated changes in the C–H stretching peaks and gradually increased the intensity of the W–O stretching peaks as the bilayer number of $WO_{2.72}$ NRs increased. These phenomena indicated the vertical growth of $(WO_{2.72}$ NR/TREN$)_n$ multilayers through a ligand-exchange reaction during consecutive LbL depositions.

UV-vis absorbance spectra of $(WO_{2.72}$ NR/TREN$)_n$ multilayers on quartz glasses also qualitatively confirmed the uniform and regular growth of multilayers with an increase in the bilayer number (n) (Fig. 3b). In addition, quantitative mass changes in the $(WO_{2.72}$ NR/TREN$)_n$ multilayers were monitored using quartz crystal microgravimetry (QCM). Fig. 2c shows the changes in the frequency ($-\Delta F$) and mass (Δm) as $WO_{2.72}$ NRs and TREN were alternately adsorbed onto QCM electrodes as a function of the bilayer number. In this case, the mass changes were calculated from the frequency changes, assuming that the formed multilayers were rigid, evenly distributed, and sufficiently thin to satisfy the Sauerbrey equation (see the detailed explanation in the Experimental section). Alternating depositions of $WO_{2.72}$ NRs and TREN resulted in a $-\Delta F$ of 81.5 ± 5.0 Hz ($\Delta m \sim 1.4 \pm 0.1$ μg cm^{-2}) per bilayer number. In particular, the decrease in Δm occurring during the deposition of TREN implied that bulky OAm ligands loosely bound to the surface of the $WO_{2.72}$ NRs were replaced by relatively small TREN molecules. Additionally, the total thickness of the $(WO_{2.72}$ NR/TREN$)_n$ multilayers increased from 28 to 116 nm as the bilayer number increased from 10 to 40, forming a highly uniform but intertwined net-like surface morphology (Fig. 3d and e and S2, S3†). Notably, the LbL-assembled $(WO_{2.72}$ NR/TREN$)_n$ multilayers exhibited a mass density of 5.40 g cm^{-3} with a porosity of 25.0% (mass density of bulk $WO_{2.72} \sim 7.21$ g cm^{-3}). These results suggest the possibility that the porous structure of the $(WO_{2.72}$ NR/TREN$)_n$ multilayers can effectively provide vacant sites for incorporating additional conductive components into EC films as well as facile pathways for Li^+ ion diffusion (*i.e.*, lithiation/delithiation) during repetitive EC operation.

3.2. Electrochemical and EC properties of $WO_{2.72}$ NR-based EC films

To demonstrate Li^+ ion intercalation for EC operation, the intrinsic electrochemical properties of $WO_{2.72}$ NR-based EC films (*i.e.*, $(WO_{2.72}$ NR/TREN$)_n$ multilayers) were evaluated using a three-electrode cell configuration in a 1 M solution of lithium perchlorate ($LiClO_4$) in propylene carbonate. First, cyclic voltammetry (CV) scans of the $(WO_{2.72}$ NR/TREN$)_n$ multilayers were acquired at a scan rate of 20 mV s^{-1} in the potential range from −1.0 to +1.0 V and analyzed as a function of the bilayer number (n) (Fig. 4a). The anodic and cathodic current levels of the asymmetric CV curves were gradually enhanced with an increase in the bilayer number (or loading amount) of the $WO_{2.72}$ NRs. In particular, the cathodic sweeps showed distinct reduction peaks related to the insertion of Li^+ ions (*i.e.*, the reduction reaction from $WO_{2.72}$ to $Li_yWO_{2.72}$ in eqn (1)),[19,53] and these peaks were slightly shifted toward a higher absolute potential with an increase in the bilayer number. These phenomena were caused by the increased total resistance in the $(WO_{2.72}$ NR/TREN$)_n$ multilayers with an increase in the loading amount of the $WO_{2.72}$ NRs, which is a well-known intrinsic property of transition metal oxides with poor electrical conductivity.[54] The total charge densities (mC cm^{-2}) of the $(WO_{2.72}$ NR/TREN$)_n$ multilayers were also measured by integrating the inner area of the CV curves (Fig. 4b). In this case, the charge densities were almost linearly increased from 0.07 to 0.40 mC cm^{-2} as the bilayer number increased from 5 to 40, implying that the charge-storage capacity of the multilayers could be further enhanced and precisely controlled by adjusting the bilayer number. Furthermore, the $(WO_{2.72}$ NR/TREN$)_{20}$ multilayers displayed good pseudocapacitive behavior at scan rates ranging from 10 to 100 mV s^{-1}, suggesting that the $WO_{2.72}$ NR-based EC films possessed a relatively good charge insertion/extraction properties and consequently a good rate capability (Fig. 4c). Electrochemical impedance spectroscopy (EIS) analyses were also performed to elucidate the resistances in the $WO_{2.72}$ NR-based EC films (Fig. 4d). In this case, we observed longer semicircular arches in the middle-frequency region as well as lower slopes of the linear tails in the low-frequency region (Warburg impedance) with an increase in the bilayer number. These results showed that the charge transfer resistance (R_{ct}) and ion diffusion resistance in $WO_{2.72}$ NR-based EC films increased with an increase in the loading amount of $WO_{2.72}$ NRs. When $(WO_{2.72}$ NR/TREN$)_n$ multilayers are applied to EC devices, these bilayer number (or loading amount/thickness)-dependent electrochemical properties, such as charge-storage capacity and total resistance, can be directly correlated with the extent of reversible color changes and switching times for coloration/bleaching. That is, increasing the bilayer number of $(WO_{2.72}$ NR/TREN$)_n$ multilayers can contribute to deeper color changes by improving their charge-storage capacity and also leads to slower switching times due to the increased total resistance within the EC films.

To more clearly confirm these possibilities, we investigated the EC performance of $WO_{2.72}$ NR-based EC films. Fig. 5a

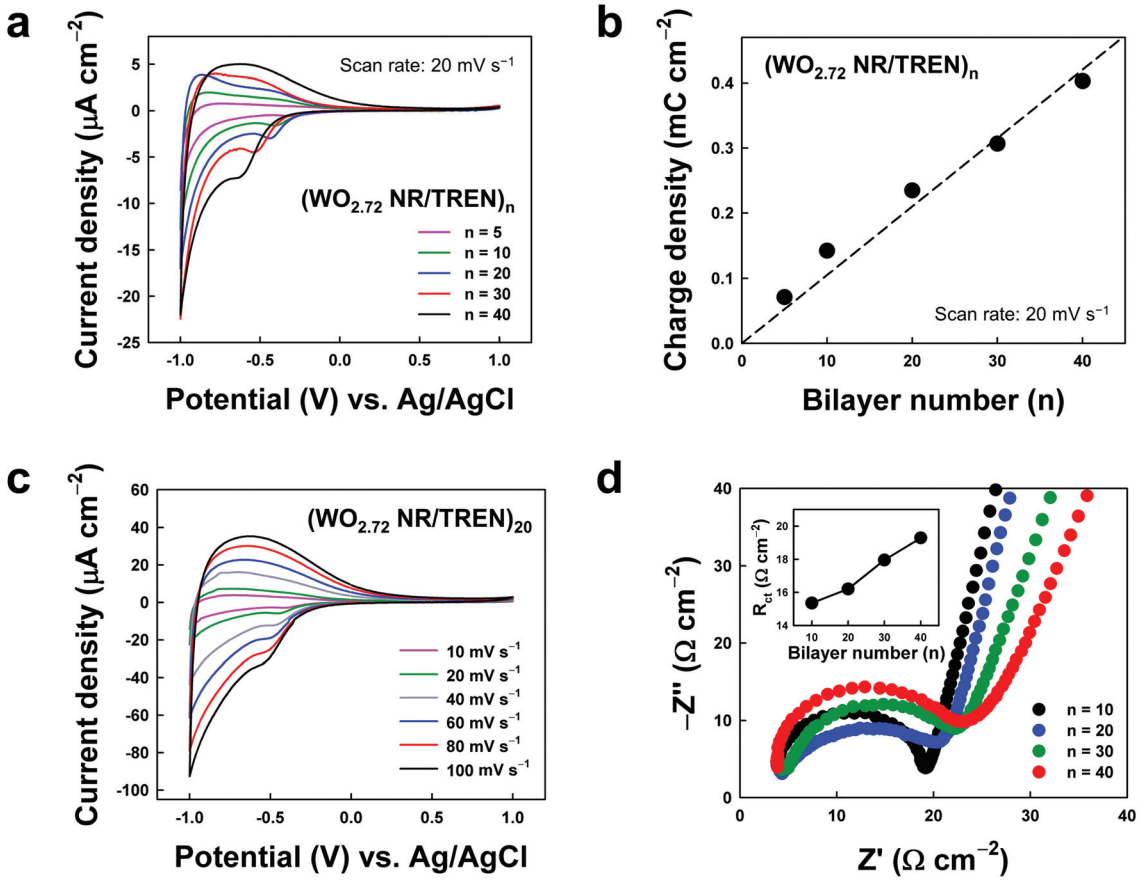

Fig. 4 (a) Cyclic voltammograms and (b) charge densities of $(WO_{2.72}$ NR/TREN$)_n$ multilayers at a scan rate of 20 mV s^{-1} as a function of the bilayer number (n). (c) Cyclic voltammograms of $(WO_{2.72}$ NR/TREN$)_{20}$ multilayers at different scan rates ranging from 10 to 100 mV s^{-1}. (d) Nyquist plots and charge transfer resistances (R_{ct}; inset) of $(WO_{2.72}$ NR/TREN$)_n$ multilayers as a function of bilayer number.

shows the optical transmittance spectra of $(WO_{2.72}$ NR/TREN$)_n$ multilayers under the applied potentials of +4.0 V (bleached state) and −4.0 V (colored state) as a function of the bilayer number (n). The $(WO_{2.72}$ NR/TREN$)_n$ multilayers in the bleached state displayed good transparency (>80.0%) in the range of 450–700 nm, covering most of the visible light region. As the bilayer number increased from 10 to 40, the optical modulation (ΔT, *i.e.*, variations in the transmittance between the bleached state and the colored state) at a visible wavelength of 633 nm increased from 26.3 to 50.3% (Fig. 5b). Additionally, this optical modulation could be controlled by changing the external potential from −1.0 V to −4.0 V (Fig. S4†). In particular, the larger changes in the transmittance by switching the applied potentials from −3.0 V to −4.0 V occurred compared to the changes at less negative potentials, which was prominently featured as the bilayer number (or film thickness) increased. This phenomenon implied that Li^+ ions were sufficiently diffused into the EC films for intercalation below −3.0 V. Deeper bluish color changes in the $(WO_{2.72}$ NR/TREN$)_n$ multilayers as the bilayer number increased were also clearly observed from photographic images (Fig. 5c). EC switching tests of $WO_{2.72}$ NR-based EC films were performed to estimate their response times for coloration/bleaching (Fig. 5d). First, the corresponding optical transmittance values at a wavelength of 633 nm during coloration (−4.0 V) and bleaching (+4.0 V) were recorded in real time. In this case, the coloration time ($t_{c,90\%}$) and bleaching time ($t_{b,90\%}$) are defined as the times required to reach 90.0% of color changes in the entire optical modulation. As a result, the $t_{c,90\%}/t_{b,90\%}$ values of the $(WO_{2.72}$ NR/TREN$)_n$ multilayers were found to be approximately 7.8 s/1.6 s (n = 10), 12.2 s/6.5 s (n = 20), 34.5 s/46.9 s (n = 30), and 44.2 s/53.2 s (n = 40) (Fig. 5e). We also examined the coloration efficiencies (CEs) of $WO_{2.72}$ NR-based EC films to determine the change in the optical density over the injected charge density during EC switching from the bleached state to the colored state using the following equation:[5]

$$\text{Coloration efficiency (CE)} = \frac{\Delta \text{OD}}{\Delta Q} = \frac{\log\left(\frac{T_b}{T_c}\right)}{\Delta Q} \quad (4)$$

In eqn (4), ΔOD, ΔQ, T_b, and T_c denote the change in optical density, the injected charge density, the transmittance in the bleached state, and transmittance in the colored state, respectively. The CEs were obtained from the slopes of lines fitted to the linear region of the plots of optical density *versus* injected charge density during coloration. As shown in Fig. 5f,

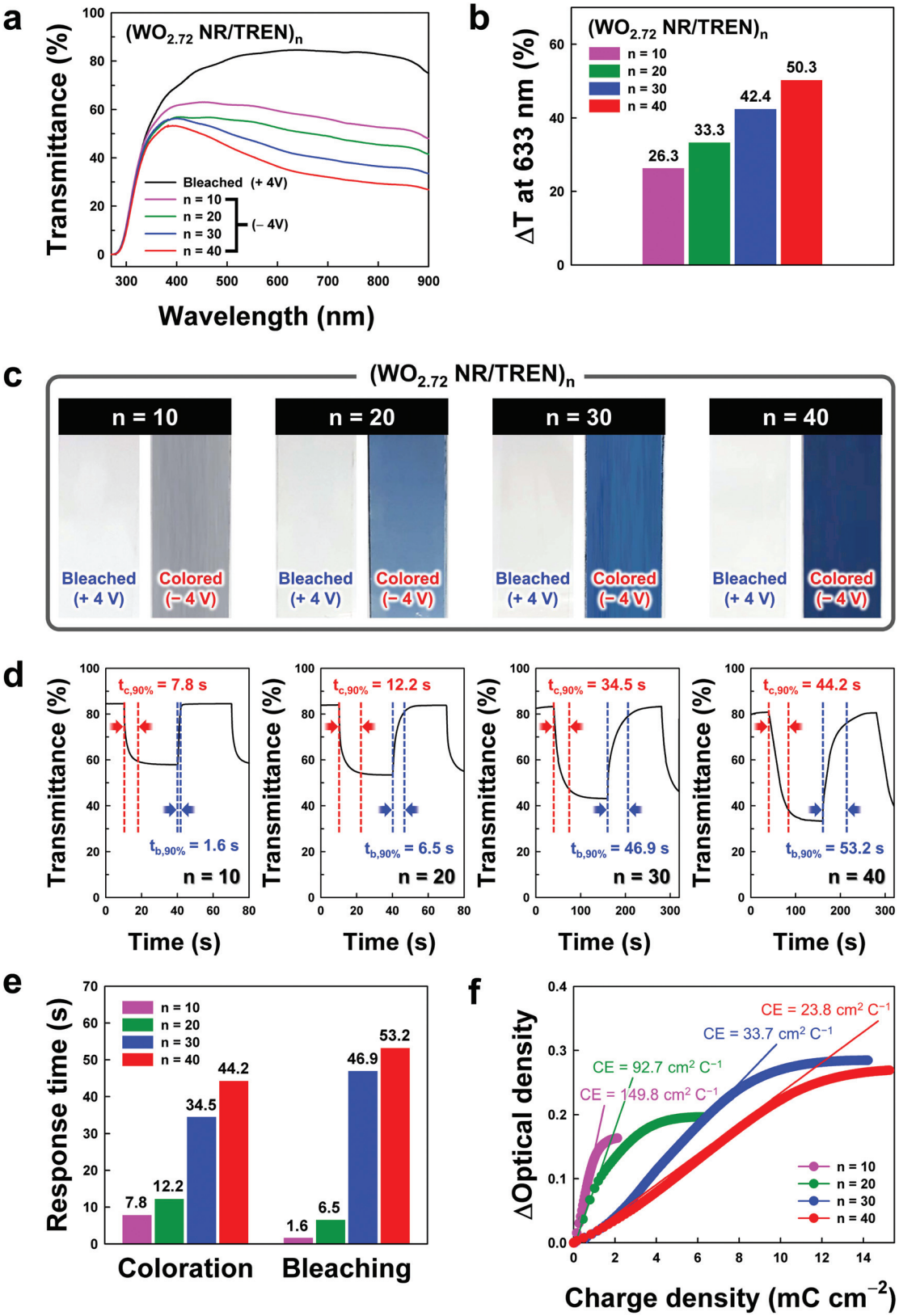

Fig. 5 (a) Optical transmittance spectra of $(WO_{2.72}$ NR/TREN$)_n$ multilayers under applied potentials of +4.0 V (bleached state) and −4.0 V (colored state) as a function of the bilayer number (n). (b) Optical modulation (ΔT) of $(WO_{2.72}$ NR/TREN$)_n$ multilayers at a visible wavelength of 633 nm as a function of the bilayer number. (c) Photographic images of $(WO_{2.72}$ NR/TREN$)_n$ multilayers in the bleached state and colored state. (d) EC switching and response times of $(WO_{2.72}$ NR/TREN$)_n$ multilayers with increasing the bilayer number from 10 to 40. (e) Coloration and bleaching times of $(WO_{2.72}$ NR/TREN$)_n$ multilayers from EC switching as a function of the bilayer number. (f) CEs of $(WO_{2.72}$ NR/TREN$)_n$ multilayers as a function of the bilayer number.

the $(WO_{2.72}$ NR/TREN$)_{10}$ multilayers exhibited a high CE (149.8 cm^2 C^{-1}), but the CEs sharply decreased down to 23.8 cm^2 C^{-1} as the bilayer number increased from 10 to 40. Considering that the charge-storage capacity and total resistance of $WO_{2.72}$ NR-based EC films are closely related to the loading amount of $WO_{2.72}$ NRs, it stands to reason that the optical modulation was improved, whereas the switching times and CEs were increased with an increase in the bilayer number. Additionally, we investigated the EC stability of $WO_{2.72}$ NR-based EC films by alternately and continuously applying potentials of ±4.0 V for 30 s intervals (Fig. S5†). The $(WO_{2.72}$ NR/TREN$)_{20}$ multilayers maintained 90.1% of their initial current after repeated EC operation for 6000 s, implying that LbL-assembled EC films bridged by small organic molecule linkers have good operational stability.

Although the total resistance in $WO_{2.72}$ NR-based EC films increased with an increase in the bilayer number of $WO_{2.72}$ NRs, it should be noted that the degradation of EC performance by increased resistance was partially mitigated by modifying the interfaces of the nanocomposites. More specifically, the charge transport length was considerably reduced by both removing the bulky/insulating OAm ligands and minimizing the separation distance between neighboring $WO_{2.72}$ NRs through the introduced small TREN molecules, which have a significant effect on the electrochemical/EC performance of $WO_{2.72}$ NR-based EC films. To confirm this possibility, we prepared $(WO_{2.72}$ NR/polymer$)_n$ multilayers using bulky amine-functionalized polyethyleneimine (PEI, $M_w \sim 50\,000$) polymers for comparison with the $(WO_{2.72}$ NR/TREN$)_n$ multilayers (TREN, $M_w \sim 146$) (Fig. 6a). As confirmed by the cyclic voltammograms acquired at a scan rate of 100 mV s^{-1} (Fig. 6b), the $(WO_{2.72}$ NR/PEI$)_{20}$ multilayers exhibited inferior current responses with weakened reduction peaks in stark contrast to those of the $(WO_{2.72}$ NR/TREN$)_{20}$ multilayers. These poor charge transport properties of the $(WO_{2.72}$ NR/PEI$)_{20}$ multilayers were also observed in the CV curves obtained with an increase in the scan rates from 10 to 100 mV s^{-1} (Fig. S6a†). For a more specific comparison, the relationship between the maximum redox peak values of the current densities (I_p) and square root of the scan rates ($v^{1/2}$) is plotted in Fig. S6b† based on the scan rate-dependent CV curves of the $(WO_{2.72}$ NR/TREN$)_n$ and $(WO_{2.72}$ NR/PEI$)_n$ multilayers (Fig. 4c and S6a†). The anodic/cathodic peak values increased linearly with increasing scan rates, indicating that the oxidation/reduction processes of $WO_{2.72}$ NRs showed diffusion-controlled behavior.[55] In particular, the relatively higher slope of I_p *vs.* $v^{1/2}$ curves obtained from the $(WO_{2.72}$ NR/TREN$)_n$ multilayers compared to that of the $(WO_{2.72}$ NR/PEI$)_n$ multilayers indicated that the small TREN linkers better facilitated charge transport within multilayers than the bulky PEI linkers. Furthermore, EIS measurements of the $(WO_{2.72}$ NR/PEI$)_{20}$ multilayers showed that the semicircular arch in the middle-frequency region tended to be stretched due to the increased charge transfer resistance, eventually making it difficult to distinguish this arch from the Warburg impedance in the low-frequency region (Fig. 6c). These results were in stark contrast with those of the $(WO_{2.72}$ NR/TREN$)_n$ multilayers, implying that the size of linkers is strongly related to the charge transfer resistance of $WO_{2.72}$ NR-based EC films. In addition to these electrochemical properties, the EC performance of $WO_{2.72}$ NR-based EC films (especially switching times for coloration/bleaching) also strongly depends on the size of the linkers bridged between neighboring $WO_{2.72}$ NRs. More specifically, the $(WO_{2.72}$ NR/PEI$)_{20}$ multilayers displayed longer response times ($t_{c,90\%} \sim 23.3$ s and $t_{b,90\%} \sim 17.6$ s) than the $(WO_{2.72}$ NR/TREN$)_{20}$ multilayers ($t_{c,90\%} \sim 12.2$ s and $t_{b,90\%} \sim 6.5$ s) in EC switching tests despite their similar optical modulations (Fig. 6d and e and S7†). In the case of CEs, the $(WO_{2.72}$ NR/PEI$)_{20}$ multilayers exhibited a lower efficiency (CE = 40.0 cm^2 C^{-1}) than the $(WO_{2.72}$ NR/TREN$)_{20}$ multilayers (CE = 92.7 cm^2 C^{-1}) (Fig. 6f). That is, the bulky PEI linkers induced a longer separation distance between adjacent $WO_{2.72}$ NRs and therefore impeded charge transport. On the other hand, the minimized separation distance between $WO_{2.72}$ NRs realized by TREN linkers could enhance the electrochemical/EC performance of EC films by reducing the numerous contact resistances at interfaces (or charge transfer resistance).

3.3. Incorporation of ITO NPs into $WO_{2.72}$ NR-based EC films

Based on these results, we tried to further enhance the EC performance of $WO_{2.72}$ NR-based EC films by the addition of transparent/conductive ITO NPs. To this end, ITO NPs, as conductive components, were periodically inserted between the respective $WO_{2.72}$ NR layers (*i.e.*, $(WO_{2.72}$ NR/TREN/ITO NP/TREN$)_m$ multilayers) to decrease the charge transfer resistance, and, simultaneously, to minimize the decrease in the optical transmittance according to the additional insertion of conductive components (Fig. 7a). First, we synthesized OAm-ITO NPs with a diameter of 7.0 ± 1.5 nm and highly stable dispersibility in toluene or hexane (Fig. 7b).[48] We also confirmed that these OAm-ITO NPs could be LbL-assembled with TREN molecules through the same ligand-exchange reaction as previously mentioned (Fig. S8†). Additionally, as shown in UV-vis absorbance and QCM analyses with an increase in the periodic number (m) (Fig. 7c and d), the alternating deposition of $WO_{2.72}$ NRs and ITO NPs using TREN linkers induced the regular and constant growth of multilayers, which generated a similar adsorption amount of $WO_{2.72}$ NRs ($-\Delta F \sim 85.0 \pm 3.5$ Hz and $\Delta m \sim 1.5 \pm 0.1$ μg cm^{-2}) as $(WO_{2.72}$ NR/TREN$)_n$ multilayers. In particular, ITO NPs with a small diameter of approximately 7.0 nm were effectively incorporated into the nanopores of $WO_{2.72}$ NR-based EC films, and the formed multilayers still displayed nanoporous structures (Fig. 7e and S9†). The cross-sectional FE-SEM image and energy-dispersive X-ray spectroscopy (EDS) mapping images of the $(WO_{2.72}$ NR/TREN/ITO NP/TREN$)_{20}$ multilayers also proved the uniform and homogeneous insertion of ITO NPs into $WO_{2.72}$ NR-based EC films (Fig. 7f). Furthermore, these results imply that the formed LbL-assembled nanocomposite film has a highly nanoblended and mixed structure instead of sharp interfaces between the $WO_{2.72}$ NR and ITO layers, which have also been demonstrated

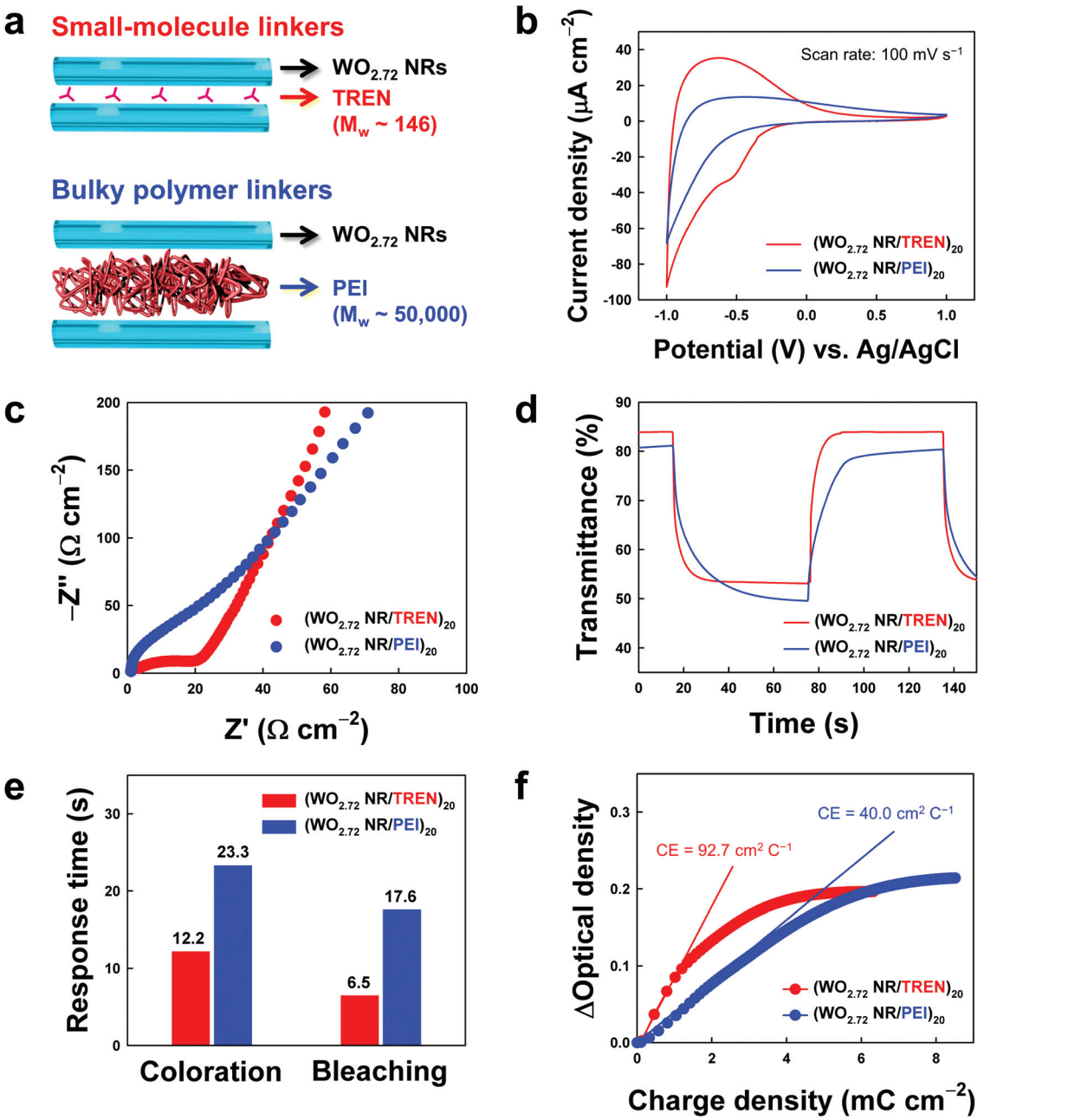

Fig. 6 (a) Schematic illustration of small-molecule linkers (TREN, M_w ~ 146) and bulky polymer linkers (PEI, M_w ~ 50 000) that bridge $WO_{2.72}$ NRs. (b) Cyclic voltammograms at a scan rate of 100 mV s^{-1} and (c) Nyquist plots of $(WO_{2.72}$ NR/TREN$)_{20}$ and $(WO_{2.72}$ NR/PEI$)_{20}$ multilayers. Comparison of (d) EC switching behaviors, (e) response times for coloration/bleaching, and (f) CEs between $(WO_{2.72}$ NR/TREN$)_{20}$ and $(WO_{2.72}$ NR/PEI$)_{20}$ multilayers.

by many other research groups related to the LbL assembly (see Fig. 1).[56–58]

A valuable benefit of the incorporated ITO NPs is the significant improvement in the overall electrochemical and EC performance of $WO_{2.72}$ NR-based EC films with ITO NPs compared to EC films without ITO NPs. For comparison, we conducted CV measurements of $(WO_{2.72}$ NR/TREN/ITO NP/TREN$)_{m=20}$ and $(WO_{2.72}$ NR/TREN$)_{n=20}$ multilayers at a scan rate of 100 mV s^{-1} in the potential range from −1.0 V to +1.0 V (Fig. 8a). The current responses of the ITO NP-incorporated EC film (charge density ~5.28 mC cm^{-2}) were notably enhanced in comparison with those of the ITO NP-free EC film (charge density ~0.31 mC cm^{-2}) even though the EC films have the same number of $WO_{2.72}$ NR layers. This superior current response of the ITO NP-incorporated EC film was also confirmed at different scan rates ranging from 10 to 100 mV s^{-1} (Fig. S10†). Although the increased current levels of the ITO NP-incorporated EC film were partially caused by the electrical

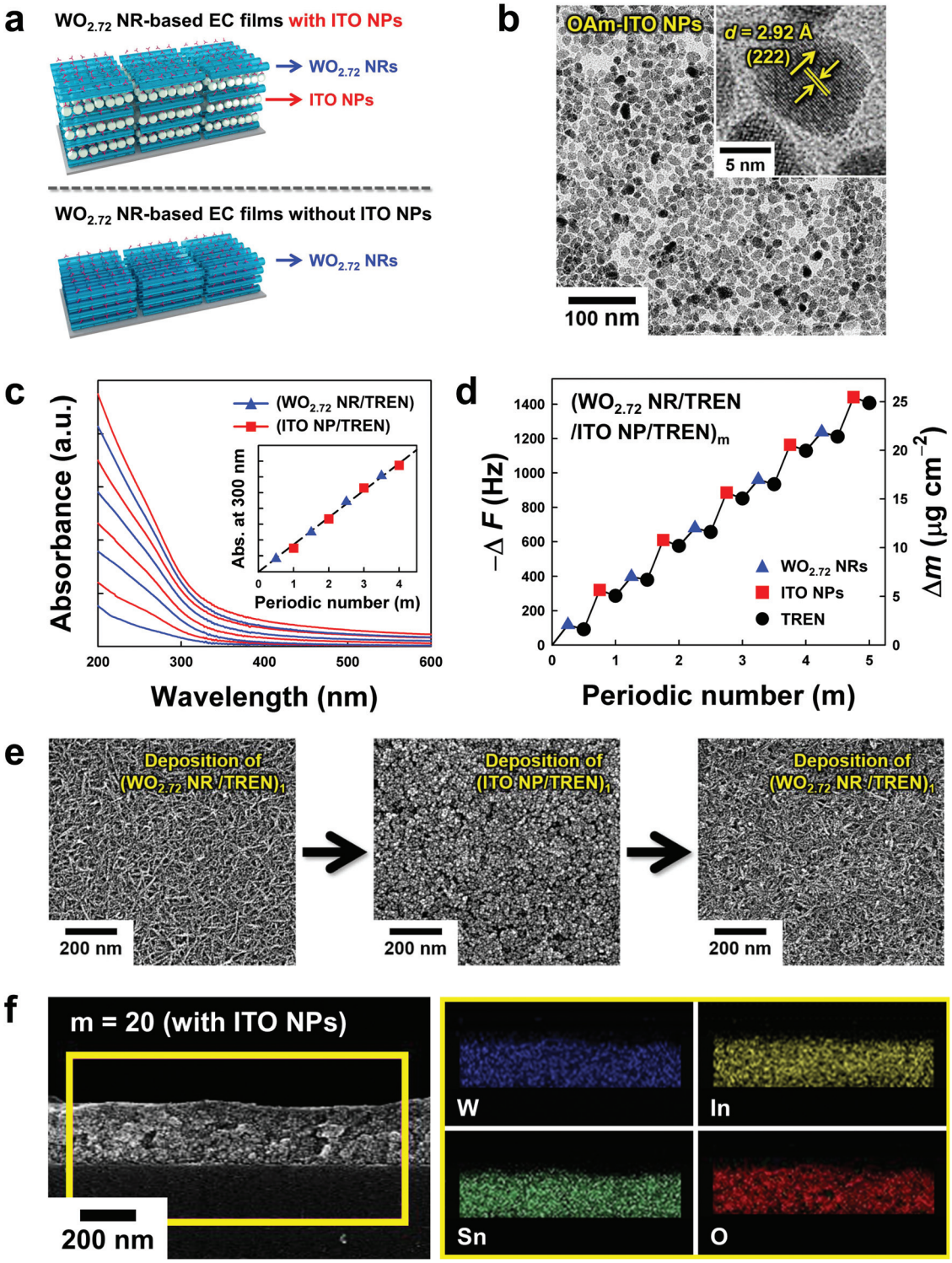

Fig. 7 (a) Schematic illustration of $WO_{2.72}$ NR-based EC films with the insertion of transparent/conductive ITO NPs. (b) HR-TEM images of OAm-ITO NPs with the (222) plane (lattice spacing (d) ~2.92 Å). (c) UV-vis absorbance spectra and (d) QCM analysis of $(WO_{2.72}$ NR/TREN/ITO NP/TREN$)_m$ multilayers as a function of the periodic number (m). (e) Planar FE-SEM images after the sequential deposition of $(WO_{2.72}$ NR/TREN$)_1$, (ITO NP/TREN$)_1$, and $(WO_{2.72}$ NR/TREN$)_1$. (f) Cross-sectional FE-SEM and EDS mapping images of $(WO_{2.72}$ NR/TREN/ITO NP/TREN$)_{20}$ multilayers.

double-layer properties of the ITO NPs (Fig. S11a†), the insertion of conductive ITO NPs within a porous EC film could also substantially reduce the total resistance, thereby facilitating charge transport. This assumption was strongly supported by the EIS measurements, in which the ITO NP-incorporated EC film exhibited a relatively low charge transfer resistance

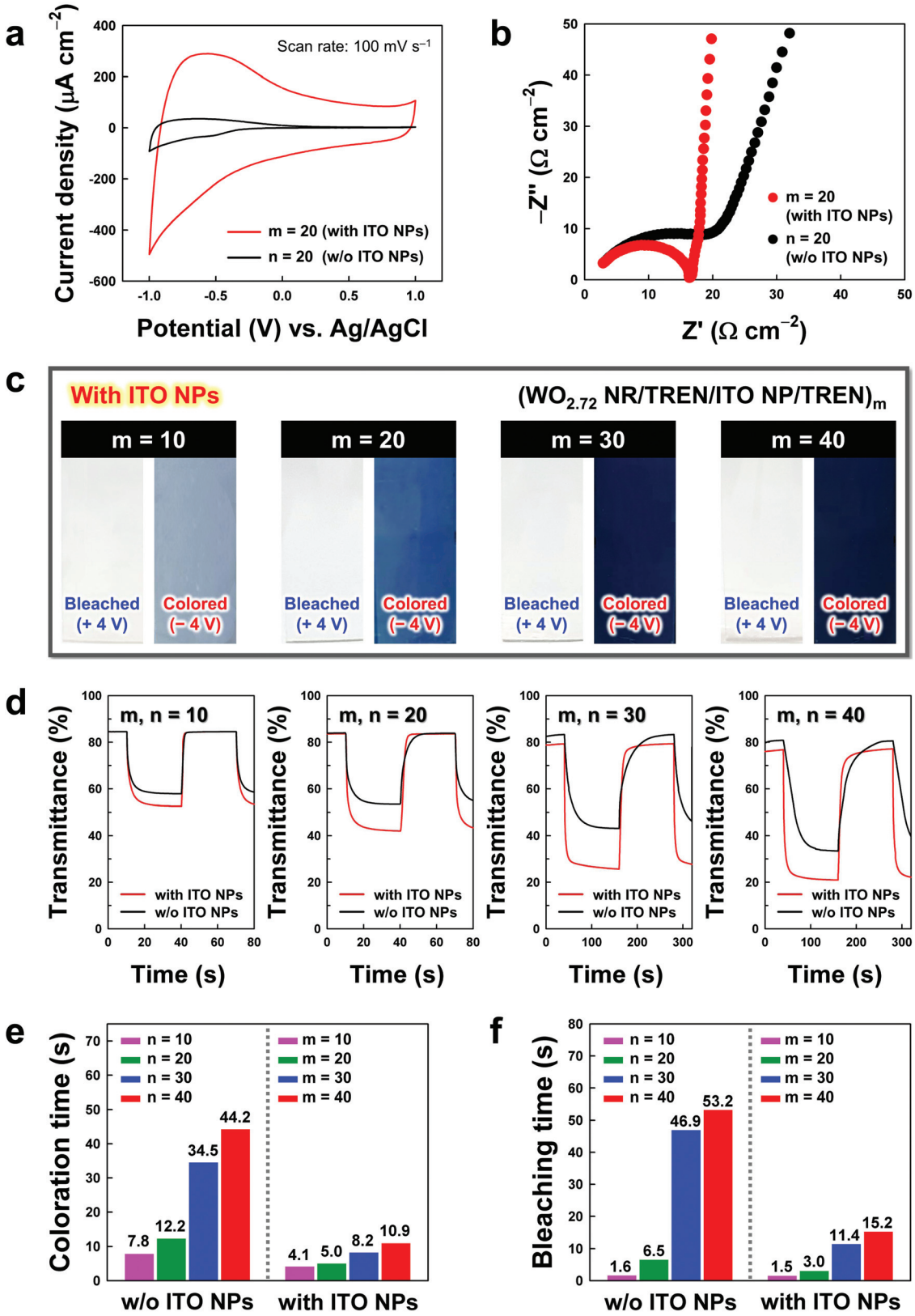

Fig. 8 (a) Cyclic voltammograms at a scan rate of 100 mV s^{-1} and (b) Nyquist plots of $WO_{2.72}$ NR-based EC films with ITO NPs (m = 20) and without ITO NPs (n = 20). (c) Photographic images of $(WO_{2.72}$ NR/TREN/ITO NP/TREN$)_m$ multilayers under applied potentials of +4.0 V (bleached state) and −4.0 V (colored state) as a function of the periodic number (m). Comparison of (d) EC switching behaviors, (e) coloration time, and (f) bleaching time between $WO_{2.72}$ NR-based EC films with ITO NPs and those without ITO NPs with the same number of $WO_{2.72}$ NR layers.

(13.5 Ω cm^{-2}) compared to that of the ITO NP-free EC film (16.2 Ω cm^{-2}) (Fig. 8b and S11b†). These results evidently showed that the periodic insertion of conductive ITO NPs within $WO_{2.72}$ NR-based EC films had notable effects on the charge transport, which is directly related to the kinetics of Li^+ ion intercalation.

Based on the improved electrochemical performance achieved by the incorporation of ITO NPs, we further examined the EC performance of $WO_{2.72}$ NR-based EC films with ITO NPs. The optical modulation of $(WO_{2.72}$ NR/TREN/ITO NP/TREN$)_m$ multilayers at a wavelength of 633 nm increased from 32.0% to 55.8% with an increase in the periodic number (m) from 10 to 40 (Fig. S12†), which corresponded to the higher values compared to those of $(WO_{2.72}$ NR/TREN$)_n$ multilayers at the same layer number of $WO_{2.72}$ NRs (Fig. S13†). Consequently, the coloration states of the ITO-incorporated EC films exhibited darker color changes than those of the ITO NP-free EC films (Fig. 8c and S14†). In particular, the ITO NP-incorporated EC films displayed a notable improvement in response times for coloration/bleaching (Fig. 8d). The coloration/bleaching times of ITO NP-incorporated EC films were found to be approximately 4.1 s/1.5 s (m = 10), 5.0 s/3.0 s (m = 20), 8.2 s/11.4 s (m = 30), and 10.9 s/15.2 s (m = 40) (Fig. 8e and f), which outperformed those of previously reported WO_x-based EC films (Table S1†). Furthermore, it is worth noting that the switching times (coloration and bleaching times) of ITO NP-incorporated EC films were remarkably faster than those of ITO NP-free EC films despite their higher optical modulation. This significant improvement in the EC performance was attributed to the enhanced charge transfer property by the incorporation of conductive ITO NPs although Li^+ ion transport can be slightly aggravated due to the increased total thickness of EC films containing ITO NP layers. Another notable feature is that the insertion of ITO NPs had little effect on the optical transmittance of the $WO_{2.72}$ NR-based EC films in the bleached state due to their inherent transparency. Given that solution-processable conductive fillers such as carbon-based materials (*e.g.*, CNTs and reduced graphene oxide (r-GO)) or metal nanomaterials are generally nontransparent, the ITO NPs can be used as a good conductive filler that can significantly reduce the charge transfer resistance across EC films, and resultantly, improve the EC performance without the loss of optical transmittance. Additionally, the CEs of the $(WO_{2.72}$ NR/TREN/ITO NP/TREN$)_m$ multilayers increased from 33.2 to 55.2 cm^2 C^{-1} as the periodic number increased from 10 to 40 (Fig. S15†). It should be noted that the incorporated ITO NPs retained a higher charge-storage capacity than the $WO_{2.72}$ NRs, and the charge stored by the ITO NPs was not used for EC operation (Fig. S11a†). Therefore, in the case of calculating the CEs of $WO_{2.72}$ NR-based EC films with ITO NPs (see eqn (4)), they have many disadvantages due to the increases in the denominator (ΔQ, charge density) caused by the charge-storage properties of the ITO NPs. However, the CEs of the ITO NP-incorporated EC films gradually increased with an increase in the periodic number from 10 to 40, which was in contrast to the CEs of the ITO NP-free EC films. In particular, the CEs of the $(WO_{2.72}$ NR/TREN/ITO NP/TREN$)_{m\ =\ 30\ and\ 40}$ multilayers were higher than those of the $(WO_{2.72}$ NR/TREN$)_{n\ =\ 30\ and\ 40}$ multilayers because the increasing effect of the numerator (ΔOD) outweighed that of the denominator (ΔQ), presumably due to the enhanced charge transport properties through the insertion of ITO NPs. Additionally, the ITO NP-incorporated EC films (m = 20) displayed a current retention of 87.3% after repetitive EC switching under alternating potentials of ±4.0 V with an interval of 30 s for 6000 s (Fig. S16†), which was similar to the results for the ITO NP-free EC films despite their higher current responses.

4. Conclusions

We reported high-performance EC films composed of electrochromic $WO_{2.72}$ NRs, transparent/conductive ITO NPs, and small-molecule linkers using an unconventional LbL assembly method. Our strategy was characterized by the fact that bulky OAm ligands bound to the surface of $WO_{2.72}$ NRs and ITO NPs are effectively replaced by amine-functionalized small molecule linkers during LbL deposition, resulting in the minimized separation distance between adjacent $WO_{2.72}$ NRs and/or ITO NPs. We also demonstrated that the periodic and effective incorporation of ITO NPs into highly porous $WO_{2.72}$ NR-based EC films significantly improved the charge transport across the EC films without the loss of optical transmittance. As a result, the synergetic effects of these approaches could significantly enhance the EC performance (mainly high optical modulation and fast switching times for coloration/bleaching) of $WO_{2.72}$ NR-based EC films. Furthermore, considering that our combined approach can be effectively applied to various functional transition metal oxide nanomaterials, this work can provide a basis for realizing a variety of electrochemical applications that require facile charge transport and optical transparency.

Conflicts of interest

The authors declare no conflict of interest.

Acknowledgements

This work was supported by the National Research Foundation (NRF) of Korea grant funded by the Ministry of Science, ICT & Future Planning (MSIP) (NRF-2018R1A2A1A05019452; NRF-2019R1A4A1027627) and the Basic Science Research Program through the National Research Foundation (NRF) of Korea funded by the Ministry of Education (NRF-2017R1A6A3A04003192).

References

1 C.-G. Granqvist, *Nat. Mater.*, 2006, **5**, 89–90.
2 M. Grätzel, *Nature*, 2001, **409**, 575–576.

3 A. Llordés, G. Garcia, J. Gazquez and D. J. Milliron, *Nature*, 2013, **500**, 323–326.
4 S. M. Islam, T. S. Hernandez, M. D. McGehee and C. J. Barile, *Nat. Energy*, 2019, **4**, 223–229.
5 Q. Zhang, C.-Y. Tsai, L.-J. Li and D.-J. Liaw, *Nat. Commun.*, 2019, **10**, 1239.
6 J. Wang, L. Zhang, L. Yu, Z. Jiao, H. Xie, X. W. Lou and X. W. Sun, *Nat. Commun.*, 2014, **5**, 4921.
7 G. Cai, J. Wang and P. S. Lee, *Acc. Chem. Res.*, 2016, **49**, 1469–1476.
8 J. Pan, Y. Wang, R. Zheng, M. Wang, Z. Wan, C. Jia, X. Weng, J. Xie and L. Deng, *J. Mater. Chem. A*, 2019, **7**, 13956–13967.
9 Y. Kim, M. Han, J. Kim and E. Kim, *Energy Environ. Sci.*, 2018, **11**, 2124–2133.
10 E. Hwang, S. Seo, S. Bak, H. Lee, M. Min and H. Lee, *Adv. Mater.*, 2014, **26**, 5129–5136.
11 R.-T. Wen, C. G. Granqvist and G. A. Niklasson, *Nat. Mater.*, 2015, **14**, 996–1002.
12 J.-L. Wang, Y.-R. Lu, H.-H. Li, J.-W. Liu and S.-H. Yu, *J. Am. Chem. Soc.*, 2017, **139**, 9921–9926.
13 A. Azam, J. Kim, J. Park, T. G. Novak, A. P. Tiwari, S. H. Song, B. Kim and S. Jeon, *Nano Lett.*, 2018, **18**, 5646–5651.
14 R.-T. Wen, G. A. Niklasson and C. G. Granqvist, *ACS Appl. Mater. Interfaces*, 2015, **7**, 28100–28104.
15 H. Zheng, J. Z. Ou, M. S. Strano, R. B. Kaner, A. Mitchell and K. Kalantar-zadeh, *Adv. Funct. Mater.*, 2011, **21**, 2175–2196.
16 S. Cong, Y. Tian, Q. Li, Z. Zhao and F. Geng, *Adv. Mater.*, 2014, **26**, 4260–4267.
17 H. Fang, P. Zheng, R. Ma, C. Xu, G. Yang, Q. Wang and H. Wang, *Mater. Horiz.*, 2018, **5**, 1000–1007.
18 S. Cong, F. Geng and Z. Zhao, *Adv. Mater.*, 2016, **28**, 10518–10528.
19 T. Kunyapat, F. Xu, N. Neate, N. Wang, A. D. Sanctis, S. Russo, S. Zhang, Y. Xia and Y. Zhu, *Nanoscale*, 2018, **10**, 4718–4726.
20 B.-R. Koo and H.-J. Ahn, *Nanoscale*, 2017, **9**, 17788–17793.
21 V. K. Thakur, G. Ding, J. Ma, P. S. Lee and X. Lu, *Adv. Mater.*, 2012, **24**, 4071–4096.
22 G. Cai, M. Cui, V. Kumar, P. Darmawan, J. Wang, X. Wang, A. L.-S. Eh, K. Qian and P. S. Lee, *Chem. Sci.*, 2016, **7**, 1373–1382.
23 R. Giannuzzi, M. Balandeh, A. Mezzetti, L. Meda, P. Pattathil, G. Gigli, F. D. Fonzo and M. Manca, *Adv. Opt. Mater.*, 2015, **3**, 1614–1622.
24 J. Xu, Y. Zhang, T.-T. Zhai, Z. Kuang, J. Li, Y. Wang, Z. Gao, Y.-Y. Song and X.-H. Xia, *ACS Nano*, 2018, **12**, 6895–6903.
25 J.-W. Liu, J. Zheng, J.-L. Wang, J. Xu, H.-H. Li and S.-H. Yu, *Nano Lett.*, 2013, **13**, 3589–3593.
26 S. Zhang, S. Cao, T. Zhang, Q. Yao, A. Fisher and J. Y. Lee, *Mater. Horiz.*, 2018, **5**, 291–297.
27 H. Li, L. McRae, C. J. Firby, M. Al-Hussein and A. Y. Elezzabi, *Nano Energy*, 2018, **47**, 130–139.
28 S. Heo, J. Kim, G. K. Ong and D. J. Milliron, *Nano Lett.*, 2017, **17**, 5756–5761.
29 H. Gu, C. Guo, S. Zhang, L. Bi, T. Li, T. Sun and S. Liu, *ACS Nano*, 2018, **12**, 559–567.
30 H. Li, L. McRae and A. Y. Elezzabi, *ACS Appl. Mater. Interfaces*, 2018, **10**, 10520–10527.
31 Z. Hu, Z. Ji, W. W. Lim, B. Mukherjee, C. Zhou, E. S. Tok and C.-H. Sow, *ACS Appl. Mater. Interfaces*, 2013, **5**, 4731–4738.
32 J. Kao, K. Thorkelsson, P. Bai, B. J. Rancatore and T. Xu, *Chem. Soc. Rev.*, 2013, **42**, 2654–2678.
33 C.-K. Lin, S.-C. Tseng, C.-H. Cheng, C.-Y. Chen and C.-C. Chen, *Thin Solid Films*, 2011, **520**, 1375–1378.
34 G. Decher, *Science*, 1997, **277**, 1232–1237.
35 B. Yeom, T. Sain, N. Lacevic, D. Bukharina, S.-H. Cha, A. M. Wass, E. M. Arruda and N. A. Kotov, *Nature*, 2017, **543**, 95–99.
36 J.-S. Lee, J. Cho, C. Lee, I. Kim, J. Park, Y.-M. Kim, H. Shin, J. Lee and F. Caruso, *Nat. Nanotechnol.*, 2007, **2**, 790–795.
37 Y. Ko, D. Shin, B. Koo, S. W. Lee, W.-S. Yoon and J. Cho, *Nano Energy*, 2015, **12**, 612–625.
38 Y. Kim, K. Y. Lee, S. K. Hwang, C. Park, S.-W. Kim and J. Cho, *Adv. Funct. Mater.*, 2014, **24**, 6262–6269.
39 Y. Song, D. Kim, S. Kang, Y. Ko, J. Ko, J. Huh, Y. Ko, S. W. Lee and J. Cho, *Adv. Funct. Mater.*, 2019, **29**, 1806584.
40 Y. Ko, H. Baek, Y. Kim, M. Yoon and J. Cho, *ACS Nano*, 2013, **7**, 143–153.
41 M. Park, Y. Kim, Y. Ko, S. Cheong, S. W. Ryu and J. Cho, *J. Am. Chem. Soc.*, 2014, **136**, 17213–17223.
42 K. E. Tettey, J. W. C. Ho and D. Lee, *J. Phys. Chem. C*, 2011, **115**, 6297–6304.
43 N. E. Dov, S. Shankar, D. Cohen, T. Bendikov, K. Rechav, L. J. W. Shimon, M. Lahav and M. E. van der Boom, *J. Am. Chem. Soc.*, 2017, **139**, 11471–11481.
44 M. Cui, W. S. Ng, X. Wang, P. Darmawan and P. S. Lee, *Adv. Funct. Mater.*, 2015, **25**, 401–408.
45 D. DeLongchamp and P. T. Hammond, *Adv. Mater.*, 2001, **13**, 1455–1459.
46 D. M. DeLongchamp, M. Kastantin and P. T. Hammond, *Chem. Mater.*, 2003, **15**, 1575–1586.
47 K. Lee, W. S. Seo and J. T. Park, *J. Am. Chem. Soc.*, 2003, **125**, 3408–3409.
48 M. Kanehara, H. Koike, T. Yoshinaga and T. Teranishi, *J. Am. Chem. Soc.*, 2009, **131**, 17736–17737.
49 Y. Li, Y. Bando and D. Golberg, *Adv. Mater.*, 2003, **15**, 1294–1296.
50 C. Guo, S. Yin, M. Yan, M. Kobayashi, M. Kakihana and T. Sato, *Inorg. Chem.*, 2012, **51**, 4763–4771.
51 B. C. Mei, K. Susumu, I. L. Medintz and H. Mattoussi, *Nat. Protoc.*, 2009, **4**, 412–423.
52 D. S. Dalavi, R. S. Devan, R. A. Patil, R. S. Patil, Y.-R. Ma, S. B. Sadale, I. Kim, J.-H. Kim and P. S. Patil, *J. Mater. Chem. C*, 2013, **1**, 3722–3728.

53 R. Giannuzzi, R. Scarfiello, T. Sibillano, C. Nobile, V. Grillo, C. Giannini, P. D. Cozzoli and M. Manca, *Nano Energy*, 2017, **41**, 634–645.
54 V. Augustyn, P. Simon and B. Dunn, *Energy Environ. Sci.*, 2014, **7**, 1597–1614.
55 P. Zhou, Z. Wan, Y. Liu, C. Jia, X. Weng, J. Xie and L. Deng, *Electrochim. Acta*, 2016, **190**, 1015–1024.
56 N. A. Kotov, I. Dekany and J. H. Fendler, *J. Phys. Chem.*, 1995, **99**, 13065–13069.
57 J. Cho, K. Char, J.-D. Hong and K. Lee, *Adv. Mater.*, 2001, **13**, 1076–1078.
58 J. Schmitt, G. Decher, W. J. Dressick, S. L. Brandow, R. E. Geer, R. Shashidhar and J. M. Calvert, *Adv. Mater.*, 1997, **9**, 61–65.